AGU PUBLICATIONS

Geophysical Research Letters

RESEARCH LETTER
10.1002/2015GL065576

Key Points:
- Confinement of lunar induced magnetic fields
- Identify favorable places to observe lunar induced magnetic fields
- Effects of lunar induced magnetic fields on the lunar plasma environment

Correspondence to:
Shahab Fatemi,
shahab@ssl.berkeley.edu

Citation:
Fatemi, S., H. A. Fuqua, A. R. Poppe, G. T. Delory, J. S. Halekas, W. M. Farrell, and M. Holmström (2015), On the confinement of lunar induced magnetic fields, *Geophys. Res. Lett.*, *42*, doi:10.1002/2015GL065576.

Received 28 JUL 2015
Accepted 18 AUG 2015
Accepted article online 24 AUG 2015

On the confinement of lunar induced magnetic fields

S. Fatemi[1,2], H. A. Fuqua[1,2], A. R. Poppe[1,2], G. T. Delory[1,2], J. S. Halekas[2,3], W. M. Farrell[2,4], and M. Holmström[5]

[1]Space Sciences Laboratory, University of California, Berkeley, California, USA, [2]Solar System Exploration Research Virtual Institute, NASA Ames Research Center, Moffett Field, California, USA, [3]Department of Physics and Astronomy, University of Iowa, Iowa City, Iowa, USA, [4]NASA Goddard Space Flight Center, Greenbelt, Maryland, USA, [5]Swedish Institute of Space Physics, Kiruna, Sweden

Abstract We examine the confinement of induced magnetic fields on the lunar dayside and nightside, when the Moon is in the solar wind. We use a three-dimensional hybrid model of plasma and place a dipole magnetic field at the center of the Moon to mimic the induced magnetic field, which is the response of the lunar interior to the time-varying interplanetary magnetic field. Consistent with previous observations and theoretical predictions, we show that the induced magnetic fields on the dayside are confined within the lunar surface through a dayside current sheet. In contrast to previous work, we show that the induced magnetic fields are not confined in the lunar wake, and they leak out, sometimes even appearing as lunar limb compressions. Finally, we identify favorable places to observe induced magnetic fields by electromagnetic sounding techniques, which will help to better constrain the lunar electrical conductivity profile, and interior structure.

1. Introduction

The interior of the Moon is crucial to comprehending fundamental processes of lunar formation and evolution, which adds insight to solar system formation. Apollo era magnetic field and seismic observations investigated the lunar interior structure and demonstrated the response of the Moon to time-varying magnetic fields [*Dyal and Parkin*, 1971; *Dyal et al.*, 1976; *Sonett*, 1982; *Nakamura et al.*, 1974, 1976]. After Apollo, Lunar Prospector, Kaguya, and Gravity Recovery and Interior Laboratory missions as well as Lunar Laser Ranging technique have considerably improved our understanding of the lunar interior [e.g., *Hood et al.*, 1999; *Williams et al.*, 2001; *Weber et al.*, 2011; *Shimizu et al.*, 2013, and *Williams et al.*, 2014].

Generally, the lunar conductivity has been estimated to increase with depth from $\sigma \ll 10^{-8}$ S/m at the surface to $\sigma \gtrsim 10^{-3}$ S/m at <900 km depth [*Dyal and Parkin*, 1971; *Dyal et al.*, 1974, 1976; *Hood et al.*, 1982; *Khan et al.*, 2006; *Grimm and Delory*, 2012]. Various measurements estimated a crust of size <60 km [*Khan*, 2002; *Lognonné et al.*, 2003; *Chenet et al.*, 2006; *Wieczorek et al.*, 2013] and suggested the presence of a core, if it exists, of radius <580 km [*Dyal and Parkin*, 1971; *Goldstein et al.*, 1976; *Russell et al.*, 1981; *Hood et al.*, 1999; *Weber et al.*, 2011; *Garcia et al.*, 2011]. However, uncertainties and limitations in measurement and analysis techniques leave open several key questions regarding the precise structure of the lunar interior [*Wieczorek et al.*, 2006; *Grimm and Delory*, 2012; *Khan et al.*, 2013].

If we assume that the Moon is a spherical object with uniform conductivity immersed in a time-varying magnetic field, the induced magnetic field can be approximated as a dipole field [*Neubauer*, 1999; *Saur et al.*, 2010]. While the Moon was in the Earth's magnetotail, Apollo subsatellite magnetic field observations estimated a lunar induced dipole moment of $-(4.23 \pm 0.64) \times 10^{14}$ A · m^2/nT, which corresponds to a core with minimum radius of 435 ± 15 km [*Russell et al.*, 1974, 1981]. Observations after Apollo, however, predicted a slightly smaller core of size $\lesssim$ 400 km [*Hood et al.*, 1999; *Shimizu et al.*, 2013]. An upper limit for the lunar core size and/or the lower mantle have also been estimated to be <1000 km from observations and theoretical calculations [*Dyal and Parkin*, 1971; *Nakamura et al.*, 1976; *Anderson*, 1983].

While the Moon is in the solar wind (nearly 70% of the time), the supersonic flow of the solar wind plasma directly impacts the lunar surface and a major fraction of it is absorbed by the Moon, leaving a plasma wake downstream with a plasma cavity (vacuum) on the nightside of the Moon [*Lyon et al.*, 1967; *Colburn et al.*, 1967]. The time-varying interplanetary magnetic field (IMF) is the main driver of inducing magnetic fields

in the conductive lunar interior. However, observations and theoretical calculations indicated that the solar wind plasma dynamic pressure on the sunlit side of the Moon is strong enough to confine any induced fields within the lunar surface [*Sonett and Colburn*, 1968; *Blank and Sill*, 1969; *Schubert et al.*, 1974]. This confinement requires a current sheet at the boundary of the resistive lunar crust and conductive plasma on the sunlit side [*Sonett and Colburn*, 1968; *Blank and Sill*, 1969]. On the antisolar side, and in the absence of plasma in the deep lunar wake, however, the induced fields are no longer confined within the lunar surface. Lunar induced magnetic fields are detected in the deep lunar wake by Apollo magnetometers on the lunar surface [*Dyal and Parkin*, 1971; *Dyal et al.*, 1974], and if the signal is strong enough, it can also be detected using electromagnetic sounding technique along low-altitude orbits [*Grimm and Delory*, 2012]. *Blank and Sill* [1969] and *Dyal and Parkin* [1971] suggested that the confinement in the wake is governed by the diamagnetic currents around the plasma cavity in the lunar wake [*Colburn et al.*, 1967; *Fatemi et al.*, 2013]; however, the confinement of the induced fields within the lunar wake is still an open question.

Here we use a three-dimensional hybrid model of plasma with a single magnetic dipole at the center of the Moon to represent induced magnetic fields and examine the confinement of lunar induced magnetic fields on the dayside and nightside of the Moon. We propose favorable places to observe lunar induced magnetic fields by electromagnetic sounding techniques.

2. Model

We use a three-dimensional hybrid plasma model where ions are treated as charged macroparticles, electrons are a massless charge-neutralizing fluid, and electric and magnetic fields are self-consistently computed from Maxwell's equations [*Holmström et al.*, 2012; *Fatemi et al.*, 2015]. We assume that the Moon is a perfect plasma absorber and is a highly resistive ($2 \times 10^7\ \Omega \cdot$ m) spherical obstacle to the solar wind. We assume that the time period of the IMF changes is very small compared to the magnetic diffusion time, which is typically greater than 3 minutes [*Blank and Sill*, 1969; *Dyal and Parkin*, 1971; *Dyal et al.*, 1974]. Therefore, we can model the induced magnetic field by placing a single magnetic dipole at the center of the Moon [*Neubauer*, 1999; *Saur et al.*, 2010]. Similar method has been successfully applied to study induced magnetic fields of Callisto [*Lindkvist et al.*, 2015]. The moment of the induced dipole field, $\mathbf{M}_{\mathrm{ind}}$, can be simplified as

$$\mathbf{M}_{\mathrm{ind}} = -\frac{2\pi}{\mu_0}\Delta\mathbf{B}\, r_c^3, \tag{1}$$

where the negative sign corresponds to the opposing magnetic field, $\Delta\mathbf{B}$ is the change in the external magnetic field (IMF), and r_c is the mean radius of an infinitely conductive sphere [*Saur et al.*, 2010].

In order to determine the distribution of IMF changes as a driver for inducing magnetic fields in the lunar interior, we used data from the Acceleration, Reconnection, Turbulence, and Electrodynamics of the Moon's Interaction with the Sun (ARTEMIS) mission [*Angelopoulos*, 2010]. ARTEMIS is a dual-probe mission in orbit around the Moon since mid-2011. We used all data from mid-2012 until mid-2015 from the ARTEMIS Fluxgate Magnetometer (FGM) [*Auster et al.*, 2008] at 4 s resolution (approximately the solar wind convection time through the Moon) to compute the magnitude of the vector change in the IMF. We selected times when both the Moon and the probes were in the solar wind and the probes were outside of the lunar wake. Figure 1a shows the distribution of IMF changes at 1 AU, normalized to the number of events per year per 1 nT bin from ARTEMIS-FGM observations. We see, for example, nearly 200 events per year were observed for 10 nT changes in the IMF. We also see that magnetic field changes >25 nT, although very rare, are possible.

Figure 1b shows the dipole moment magnitude calculated from equation (1) for $0.1\ R_L \le r_c \le 1.0\ R_L$, where $R_L = 1728$ km is the radius of the Moon, for a range of magnetic field changes shown in Figure 1a. A minimum size of the lunar core estimated by *Russell et al.* [1981] and a maximum size of the core estimated by *Dyal and Parkin* [1971] are marked with dashed lines as references.

2.1. Coordinate System and Simulation Parameters

Here we use a right-handed coordinate system centered at the Moon. The solar wind flows along the $-x$ axis, the $+z$ axis is perpendicular to the ecliptic plane and points to the ecliptic north, and the y axis completes the right-hand system. We use a $8\ R_L \times 5R_L \times 5R_L$ simulation domain with cubic cells of size $\Delta x = R_L/16$ (108 km). We use typical solar wind conditions at 1 AU where the solar wind velocity is 350 km/s, the IMF magnitude is 5 nT, the ion number density is 6 cm^{-3}, and the ion and electron temperatures are 6 eV and 10 eV, respectively. The

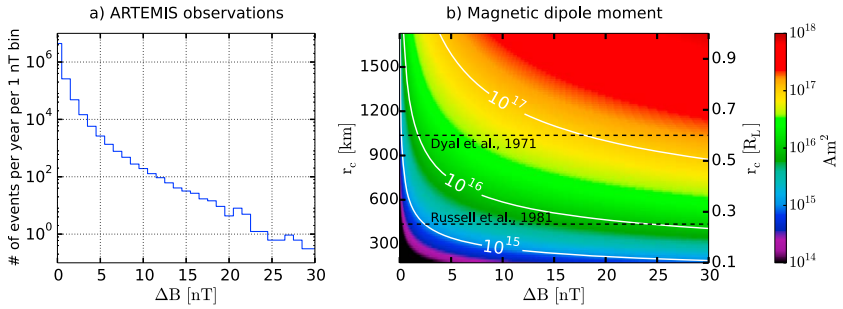

Figure 1. (a) ARTEMIS-FGM observations of magnetic field changes at 1 AU from mid-2012 to mid-2015, normalized to the number of events per year per 1 nT bin, when both the Moon and ARTEMIS probes were in the solar wind and ARTEMIS probes were outside the lunar wake. (b) Magnitude of the magnetic moment obtained from equation (1) for the mean radius of a conductive sphere $0.1R_L \leq r_c \leq 1.0R_L$, where $R_L = 1728$ km is the radius of the Moon. The white lines indicate the magnetic moment magnitudes applied in our simulations (see Table 1) and their corresponding mean radius of a conductive sphere (r_c) and external magnetic field changes (ΔB). Two dashed lines mark the minimum and maximum lunar core sizes estimated from Apollo magnetic field observations by *Russell et al.* [1981] and *Dyal and Parkin* [1971], respectively.

corresponding fast magnetosonic Mach number is ~5.6, and both the sonic and Alfvénic Mach numbers are ~8.0. These parameters are applied to the inflow boundary (*yz* plane at $x = +2.0R_L$) of our simulation domain, and they remain constant during the simulations. In our model, the simulation time step is $\Delta t < \mu_0 \Delta x^2 / 2\eta$, where $\mu_0 = 4\pi \times 10^{-7}$ H · m and $\eta = 2 \times 10^7\ \Omega \cdot$ m is the resistivity of the Moon, then $\Delta t < 3.6 \times 10^{-4}$ s. We could not choose η larger than $2 \times 10^7\ \Omega \cdot$ m due to computational constraints. However, $\eta = 2 \times 10^7\ \Omega \cdot$ m is large enough not to influence the plasma environment around the Moon. We present the results after our simulations reached a steady state (t = 80 s). For more details about our model, see *Holmström et al.* [2012] and *Fatemi et al.* [2015].

As summarized in Table 1, we constructed a series of simulation runs using two extreme IMF angles: perpendicular (along the +*y* axis) and antiparallel (along the +*x* axis) to the solar wind flow. For both of the IMF directions, we ran one simulation without a dipole field (runs #A1 and #B1), one simulation with a magnetic dipole $|\mathbf{M}_{\text{ind}}| = 10^{16}$ A · m^2 antialigned to the IMF (runs #A2 and #B2) and one simulation perpendicular to the IMF direction (runs #A3 and #B3). This magnetic moment magnitude corresponds to, for example, r_c = 580 km and $|\Delta \mathbf{B}| \simeq 10$ nT, which is equivalent to 10^{15} A · m^2/nT, consistent with observations [*Russell et al.*, 1974, 1981; *Hood et al.*, 1999]. ARTEMIS observations at 1 AU (Figure 1a) show that 10 nT IMF changes are quite common in the solar wind (~200 events per year). Since the moon is not a ferromagnetic object [*Dyal et al.*, 1974], the assumption of linear proportionality between the magnetization and the applied magnetic field is a valid assumption [*Tauxe et al.*, 2014].

Table 1. Magnitude and Direction of the Induced Dipole Moment Applied in Our Simulation Runs (See Section 2.1 for All Other Upstream Parameters)

Run	Dipole Moment (A · m^2)	IMF Direction $(\hat{b}_x, \hat{b}_y, \hat{b}_z)$[a]	Dipole Orientation $(\hat{m}_x, \hat{m}_y, \hat{m}_z)$[b]
#A1	0.0	(0, +1, 0)	No dipole used
#A2	10^{16}		(0, −1, 0)
#A3	10^{16}		(−1, 0, 0)
#A4	10^{15}		(0, −1, 0)
#A5	10^{17}		(0, −1, 0)
#B1	0.0	(+1, 0, 0)	No dipole used
#B2	10^{16}		(−1, 0, 0)
#B3	10^{16}		(0, −1, 0)

[a] $\hat{b}_i$ is magnetic field unit vector along the *i* axis.
[b] $\hat{m}_i$ is dipole moment unit vector along the *i* axis.

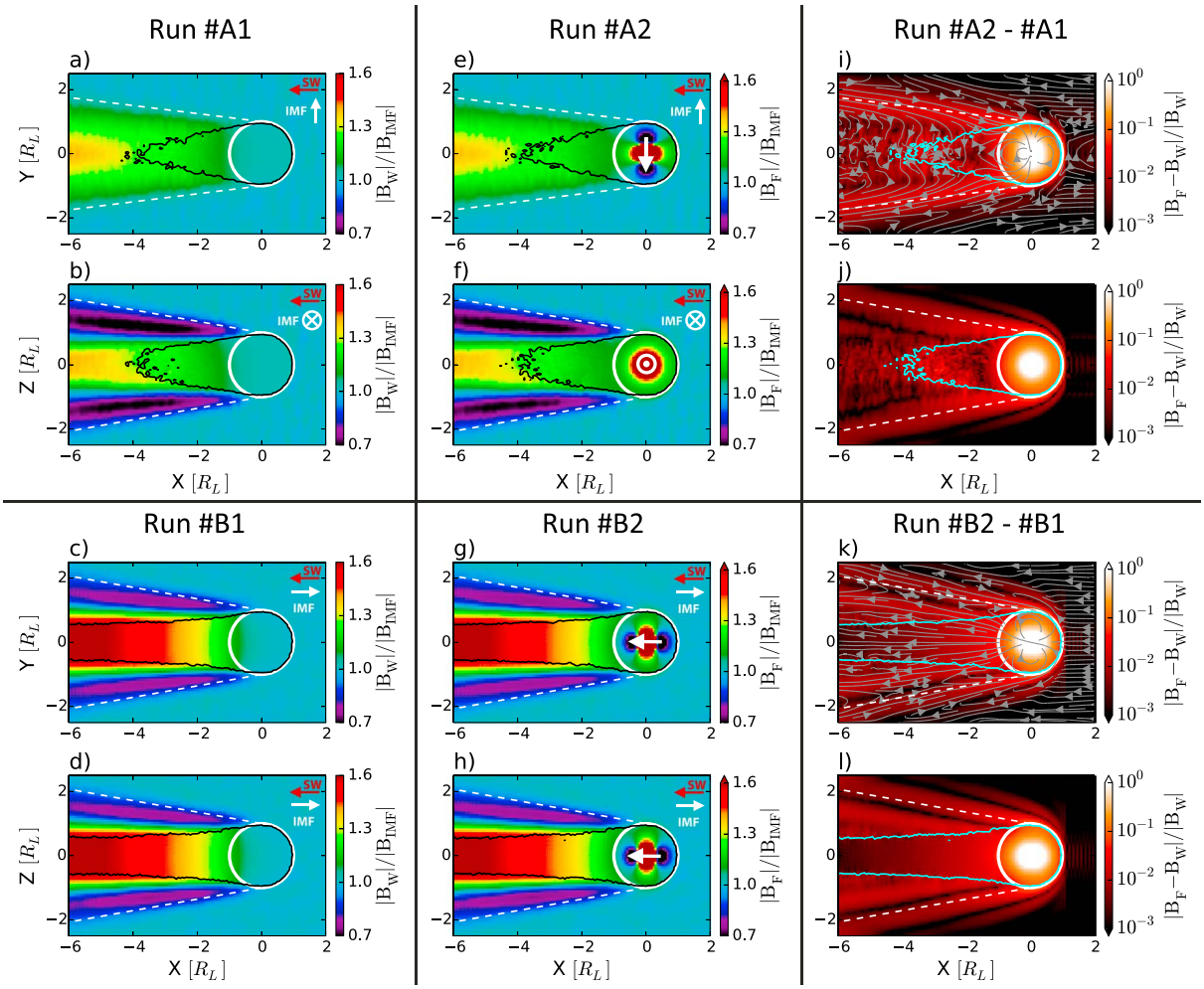

Figure 2. Magnitude of the magnetic fields obtained from hybrid simulations for (a, b) run #A1, (c, d) run #B1, (e, f) run #A2, and (g, h) run #B2, normalized to the IMF magnitude. (i–l) Magnitude of the magnetic field residuals from subtraction of Figures 2a–2d from Figures 2e–2h, normalized to the magnetic fields in Figures 2a–2d. Figures 2a, 2e, and 2i and Figures 2c, 2g, and 2k are cuts in the *xy* plane at $z = 0$, viewed from the $-y$ axis, and Figures 2b, 2f, and 2j and Figures 2d, 2h, and 2l are cuts in the *xz* plane at $y = 0$, viewed from the $+z$ axis. In all panels, the solar wind flows from the right to the left of the panel along the $-x$ axis, shown by red arrows. The direction of the IMF is shown by white arrows, and the direction of the induced dipole moment is shown at the center of the Moon. The Moon is located at the center of the coordinate system and is shown by a white circle. The boundaries of the plasma cavity (vacuum with zero plasma density) are marked by contour lines behind the Moon. The white dashed lines mark the theoretical boundaries of the lunar Mach cone (wave fronts) in different planes.

In order to investigate the effects of the dipole field strength, we also used dipole moments with $|\mathbf{M}_{ind}| = 10^{15}\,\mathrm{A}\cdot\mathrm{m}^2$ (run #A4) and $|\mathbf{M}_{ind}| = 10^{17}\,\mathrm{A}\cdot\mathrm{m}^2$ (run #A5) for the dipole opposite to the IMF direction. We marked the corresponding core size and magnetic field changes for the magnetic moments applied with white lines in Figure 1b.

3. Results

Figures 2a–2d show the normalized magnetic field magnitude ($|\mathbf{B}_W|/|\mathbf{B}_{IMF}|$) in the absence of an induced dipole from our hybrid simulation run #A1 (Figures 2a and 2b) and run #B1 (Figures 2c and 2d), where $|\mathbf{B}_W|$ is the magnitude of the magnetic field for simulation runs without a magnetic dipole and $|\mathbf{B}_{IMF}| = 5$ nT is the magnitude of the IMF in our simulations. The cuts are in the ecliptic plane (*xy* plane at $z = 0$) and in the midnight meridian plane (*xz* plane at $y = 0$). As a result of plasma absorption by the lunar surface a plasma wake forms downstream behind the Moon that perturbs magnetic fields and plasma [*Lyon et al.*, 1967; *Colburn et al.*, 1967]. These perturbations are confined within the lunar Mach cone through the lunar wake current systems [*Whang and Ness*, 1970; *Fatemi et al.*, 2013]. The theoretical boundaries of the Mach cone (characteristics of the wave fronts) are shown by the white dashed lines in Figure 2. In the IMF plane, these boundaries are

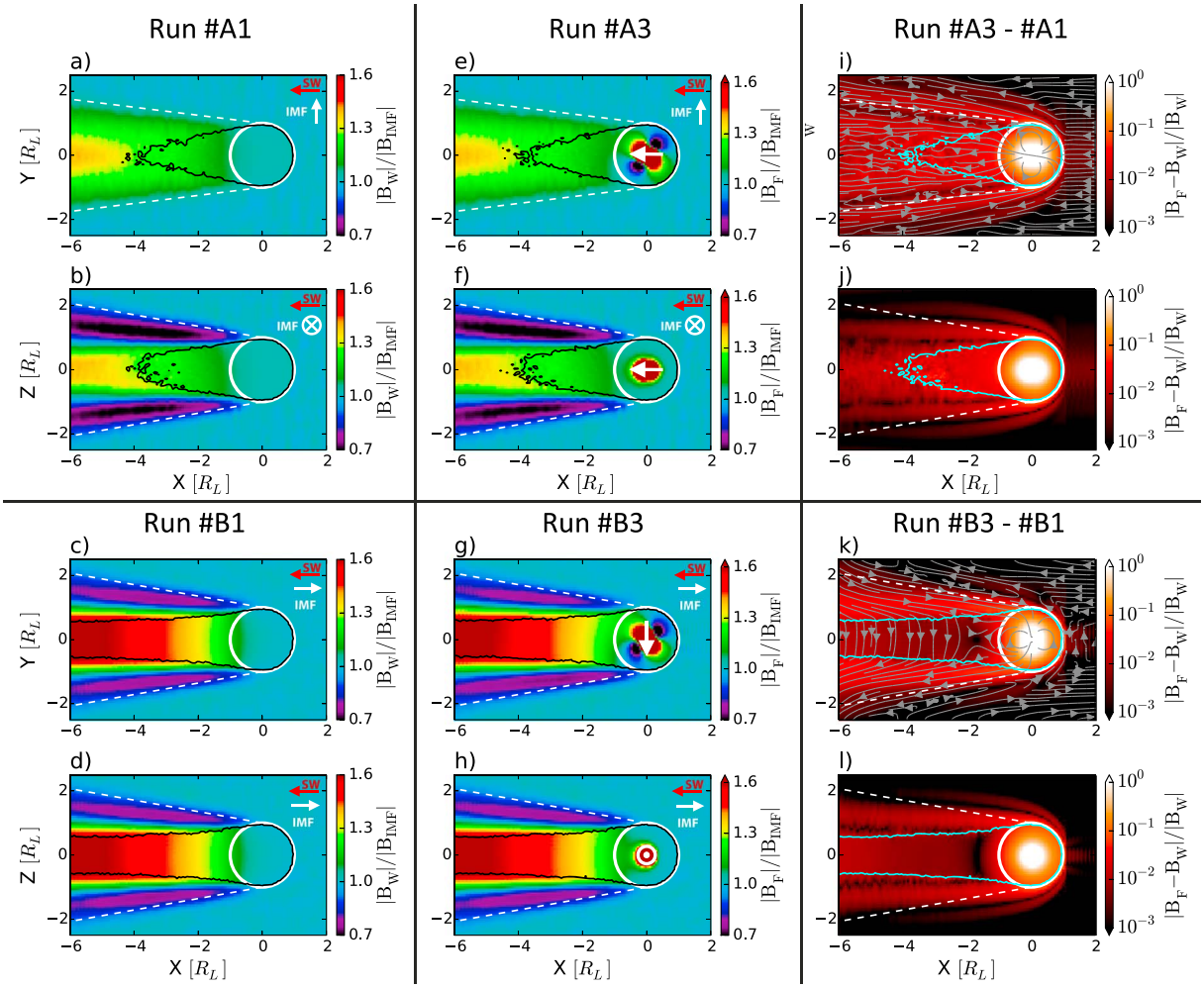

Figure 3. Normalized magnitude of the magnetic fields obtained from hybrid simulations for (a, b) run #A1, (c, d) run #B1, (e, f) run #A3, and (g, h) run #B3. (i–l) Normalized magnitude of the magnetic field residuals from subtraction of Figures 3a–3d from Figures 3e–3h. The geometry of the cuts is the same as those in Figure 2.

determined by the ion sound speed ($c_s \simeq 45$ km/s here) or the Alfvén speed ($v_A \simeq 45$ km/s here), whichever is the fastest. In a plane perpendicular to IMF, the Mach cone boundaries are determined by the fast magnetosonic speed ($v_{ms} \simeq 63$ km/s). Since the Moon in our model is a resistive obstacle without an intrinsic magnetic field and without crustal magnetizations, we see magnetic field perturbations neither on the surface of the Moon on the dayside nor in the upstream solar wind (Figures 2a–2d).

Next, we placed a magnetic dipole at the center of the Moon, representative of the lunar induced fields with $|\mathbf{M}_{ind}| = 10^{16}$A · m^2 and the normalized magnetic field magnitudes ($|\mathbf{B}_F|/|\mathbf{B}_{IMF}|$) for runs #A2 and #B2, where the dipole orientation is opposite to the IMF direction, are shown in Figures 2e–2h. Here $|\mathbf{B}_F|$ is the magnetic field magnitude of the simulation runs with a magnetic dipole. We again see the lunar wake structure downstream, and we do not observe any signature of considerable magnetic field perturbations upstream (e.g., a shock), which is consistent with observations [*Lyon et al.*, 1967]. In order to distinguish the effects of the dipole magnetic field on the global aspects of the plasma interaction with the Moon, we subtracted our simulation results without the dipole (Figures 2a–2d) from those with the dipole (Figures 2e–2h), normalized them to those without the dipole ($|\mathbf{B}_F - \mathbf{B}_W|/|\mathbf{B}_W|$), and the results are shown in Figures 2i–2l. Figures 2i–2l show that the dipole fields are confined in the lunar dayside, but they perturb the lunar wake magnetic fields, and they are not confined within the lunar Mach cone. Our simulations show that there is nearly 10% magnetic field difference due to the induced dipole fields near the Mach cone boundaries, especially at close distances to the Moon, and in the deep lunar wake. The grey contour lines in Figures 2i and 2k show that the magnetic field residuals inside the plasma cavity (marked with blue contours) have a dipole-like shape at close distances

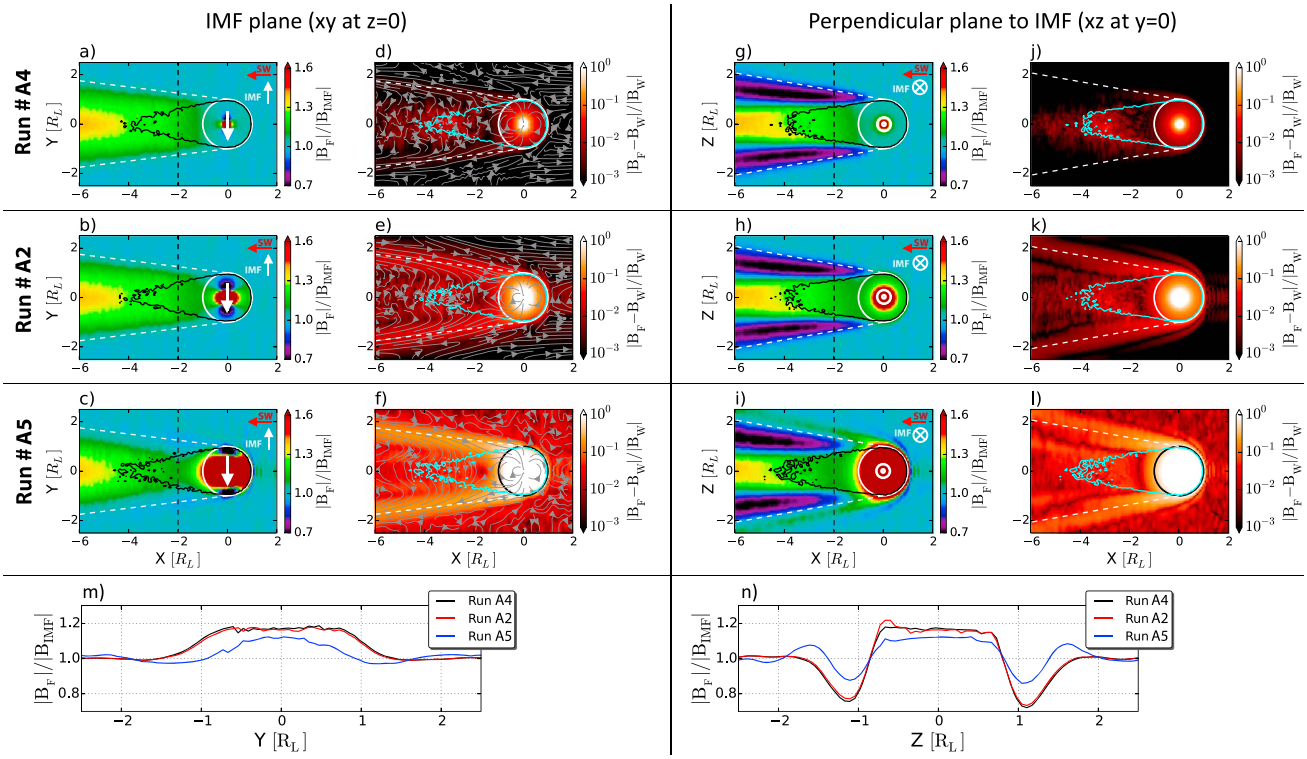

Figure 4. Normalized magnitude of the magnetic fields obtained from hybrid simulations for (a, d, g, and j) run #A4, (b, e, h, and k) run #A2, and (c, f, i, and l) run #A5. Figures 4a–4c show normalized magnetic fields in the IMF plane (*xy* plane at $z = 0$) for runs #A4, #A2, and #A5, respectively. Figures 4d–4f show normalized residual of the magnetic fields from subtraction of Figure 2a from Figures 4a–4c. Figures 4g–4i show normalized magnetic fields in a plane perpendicular to the IMF (*xz* plane at $y = 0$) for runs #A4, #A2, and #A5, respectively. Figures 4j–4l show normalized residual of the magnetic fields from subtraction of Figure 2b from Figures 4g–4i. The geometry of the cuts is the same as those in Figure 2. (m, n) Normalized magnetic field magnitude along black dashed lines at $x = -2R_L$, shown in Figures 4a–4c and 4g–4i.

to the Moon ($x > -2R_L$). However, the dipole fields are distorted outside the plasma cavity due to their interaction with the solar wind. These simulations suggest that close distances to the terminator as well as inside the plasma cavity, for the geometries presented here, are favorable places to observe lunar induced magnetic fields using electromagnetic sounding techniques.

We rotated the dipole moment 90° with respect to the IMF direction in runs #A3 and #B3, and the results are shown in Figure 3. Similar to Figure 2, Figures 3a–3d show simulation results in the absence of an induced dipole (runs #A1 and #B1). Figures 3e–3h show simulation results with a magnetic dipole for runs #A3 and #B3, and Figures 3i–3l are the residual of the magnetic fields. Similar to Figures 2i–2l, we see from Figures 3i–3l that the induced dipole fields are confined in the lunar dayside without any considerable distortion on the upstream magnetic fields, but they are not confined inside the Mach cone. Due to the dipole orientation, we see that magnetic field perturbations are more spread out over larger areas around lunar Mach cone when the dipole moment is parallel to the solar wind compared to a perpendicular dipole to the solar wind (e.g., compare Figure 2i with Figure 3i).

We compare the effects of a weaker induced dipole moment (run #A4 with $|\mathbf{M}_{ind}| = 10^{15}\,\mathrm{A \cdot m^2}$) and a stronger induced dipole moment (run #A5 with $|\mathbf{M}_{ind}| = 10^{17}\,\mathrm{A \cdot m^2}$) with what we presented earlier (run #A2 with $|\mathbf{M}_{ind}| = 10^{16}\,\mathrm{A \cdot m^2}$). We assume that the IMF is perpendicular to the solar wind and the magnetic dipole orientation is opposite to the IMF direction, and the results are presented in Figure 4. Figures 4a–4c and Figures 4g–4i compare the effects of the dipole strength on the solar wind plasma interaction with the Moon in the IMF plane (*xy* plane) and in a plane perpendicular to IMF (*xz* plane), respectively. The magnetic field residuals from subtraction of the magnetic fields when no dipole is included (run #A1) from those with the dipole (runs #A4, #A2, and #A5) in the IMF plane and in a plane perpendicular to the IMF are also shown in Figures 4d–4f and 4j–4l, respectively. When the dipole strength is small (Figures 4a, 4d, 4g, and 4j), the induced dipole fields do not have any considerable impact on magnetic field perturbations outside the Moon.

However, when the dipole fields are strong (Figures 4c, 4f, 4i, and 4l), we see large magnetic field changes around the Moon (Figures 4c and 4i), as well as strong magnetic field enhancement outside the Mach cone, similar to limb compressions [*Russell and Lichtenstein*, 1975], in a perpendicular plane to the IMF (Figure 4i).

Figures 4m and 4n compare normalized magnetic fields ($|\mathbf{B}_F|/|\mathbf{B}_{IMF}|$) in the IMF plane and in a perpendicular plane to the IMF at $x = -2R_L$ along the black dashed lines shown in Figures 4a–4c and 4g–4i, respectively. Figure 4m shows the magnetic field enhancement through the center of the wake in the IMF plane, which is consistent with observations [*Halekas et al.*, 2005; *Zhang et al.*, 2014]. It also shows that the lunar wake is distorted by the dipole fields. The black and red lines in Figure 4n indicate typical lunar wake magnetic field features from runs #A4 and #A2 [e.g., *Halekas et al.*, 2005 and *Zhang et al.*, 2014], whereas the blue line from run #A5 shows limb compression signatures outside the rarefaction region (at $z \simeq \pm 1.7\, R_L$) in addition to the typical wake magnetic field [e.g., *Russell and Lichtenstein*, 1975]. The dipole moment in run #A5 is strong enough to considerably change the global structure of the lunar wake yet does not form a bow shock. Figures 4f and 4l show that the strength of the magnetic field residuals near the lunar terminator and adjacent to the Mach cone boundary is nearly 80% of the magnetic fields without the dipole (run #A1). They also imply the presence of a large dayside current that confines the dipole fields in the lunar dayside.

4. Discussion

We used a three-dimensional hybrid plasma model to study the effects of lunar induced magnetic fields on the general aspects of plasma interaction with the Moon. We used a single dipole magnetic moment representative of the lunar induced magnetic field, and we changed the magnetic moment strength within a reasonable range to be consistent with observations (Figure 1). If the dipole moment increases too much, the interaction changes from a magnetosonic wake to a shock-like and/or magnetosphere-like interaction [*Omidi et al.*, 2002].

Our steady state simulation results show that the lunar induced magnetic field is confined within the lunar surface on the dayside (e.g., Figures 2e–2l), which is consistent with observations and theoretical predictions [*Blank and Sill*, 1969; *Schubert et al.*, 1974]. This magnetic field confinement is through a current sheet that forms between the boundary of the lunar surface and upstream plasma [*Sonett and Colburn*, 1968; *Blank and Sill*, 1969]. The model confirms the formation of this current layer to be within one simulation cell above the Moon (~100 km), which is consistent with previous observations [*Schubert et al.*, 1974]. The effects of this current on the dayside magnetic field can be seen in our simulations (e.g., Figures 4j–4l). In addition, our simulations (e.g., Figures 4k and 4l) show that lunar induced magnetic fields are confined neither within the diamagnetic currents around the plasma cavity nor inside the lunar Mach cone (wake). This is in contrast with what has been previously considered [*Blank and Sill*, 1969, Figure 5] and [*Dyal and Parkin*, 1971, Figure 2].

Our simulation results show that lunar induced magnetic field signatures can be strong around the lunar terminator, deep in the lunar wake, and near the Mach cone boundaries at close distances to the Moon ($t < 0.3R_L$), especially during large IMF changes (>10 nT), which are not rare near the Moon (Figure 1a). They also show that during large IMF changes, lunar induced magnetic fields may be observed as a limb compression outside the lunar wake (e.g., Figure 4i). Lunar limb compressions are intermittent magnetic field and plasma compressions that are often observed outside the lunar wake and are thought to be only generated by the solar wind interaction with lunar magnetic anomalies [*Russell and Lichtenstein*, 1975; *Halekas et al.*, 2008]. Our model results suggest that a secondary source of limb compressions could be the solar wind interaction with lunar induced magnetic field, if the upstream IMF changes are large.

The simulation results presented here help to determine places around the Moon that we can observe induction signals, which has a direct implication on better estimating the lunar electrical conductivity profile, on constraining interior structure, and hopefully better understanding the formation of the Moon. The results of this study also help us to distinguish lunar wake magnetic fields generated due to the dayside plasma absorption from those that are formed by the induction.

Acknowledgments

S.F., H.A.F., A.R.P., G.T.D., J.S.H., and W.M.F. gratefully acknowledge support from NASA's SSERVI institute, grant NNX14AG16A. H.A.F. work was also supported by NASA Earth and Space Science Fellowship Program, grant NESSF15. This publication is a SSERVI contribution SSERVI-2015-161. This research was conducted using resources provided by the Swedish National Infrastructure for Computing (SNIC) at the High Performance Computing Center North (HPC2N), Umeå University, Sweden. The software used in this work was developed in part by the DOE NNSA ASC-supported and DOE Office of Science ASCR-supported Flash Center for Computational Science at the University of Chicago. All ARTEMIS data used here are publicly available at http://artemis.ssl.berkeley.edu and NASA's CDAWeb.

The Editor thanks two anonymous reviewers for their assistance in evaluating this paper.

References

Anderson, K. A. (1983), Magnetic dipole moment estimates for an ancient lunar dynamo, *J. Geophys. Res.*, *88*(S02), A588–A590.

Angelopoulos, V. (2010), The ARTEMIS mission, *Space Sci. Rev.*, *165*(1–4), 3–25.

Auster, H. U., et al. (2008), The THEMIS fluxgate magnetometer, *Space Sci. Rev.*, *141*, 235–264.

Blank, J. L., and W. R. Sill (1969), Response of the Moon to the time-varying interplanetary magnetic field, *J. Geophys. Res.*, *74*(3), 736–743.

Chenet, H., P. Lognonné, M. Wieczorek, and H. Mizutani (2006), Lateral variations of lunar crustal thickness from the Apollo seismic data set, *Earth Planet. Sci. Lett.*, *243*(1–2), 1–14.

Colburn, D. S., R. G. Currie, J. D. Mihalov, and C. P. Sonett (1967), Diamagnetic solar-wind cavity discovered behind Moon, *Science*, *158*(3804), 1040–1042.
Dyal, P., and C. W. Parkin (1971), Electrical conductivity and temperature of the lunar interior from magnetic transient-response measurements, *J. Geophys. Res.*, *76*(25), 5947–5969.
Dyal, P., C. W. Parkin, and W. D. Daily (1974), Magnetism and the interior of the Moon, *Rev. Geophys.*, *12*(4), 568–591.
Dyal, P., C. W. Parkin, and W. D. Daily (1976), Structure of the lunar interior from magnetic field measurements, in *Proceedings of 7th Lunar Science Conference, Houston, Tex., March 15–19, 1976*, vol. 3, pp. 3077–3095, Pergamon Press, New York.
Fatemi, S., M. Holmström, Y. Futaana, S. Barabash, and C. Lue (2013), The lunar wake current systems, *Geophys. Res. Lett.*, *40*, 17–21, doi:10.1029/2012GL054635.
Fatemi, S., C. Lue, M. Holmström, A. R. Poppe, M. Wieser, S. Barabash, and G. T. Delory (2015), Solar wind plasma interaction with Gerasimovich lunar magnetic anomaly, *J. Geophys. Res. Space Physics*, *120*, 4719–4735.
Garcia, R. F., J. Gagnepain-Beyneix, S. Chevrot, and P. Lognonné (2011), Very preliminary reference Moon model, *Phys. Earth Planet. Inter.*, *188*(1–2), 96–113.
Goldstein, B. E., R. J. Phillips, and C. T. Russell (1976), Magnetic permeability measurements and a lunar core, *Geophys. Res. Lett.*, *3*(6), 289–292.
Grimm, R. E., and G. T. Delory (2012), Next-generation electromagnetic sounding of the Moon, *Adv. Space Res.*, *50*(12), 1687–1701.
Halekas, J. S., S. D. Bale, D. L. Mitchell, and R. P. Lin (2005), Electrons and magnetic fields in the lunar plasma wake, *J. Geophys. Res.*, *110*, A07222, doi:10.1029/2004JA010991.
Halekas, J. S., D. A. Brain, R. P. Lin, and D. L. Mitchell (2008), Solar wind interaction with lunar crustal magnetic anomalies, *Adv. Space Res.*, *41*(8), 1319–1324.
Holmström, M., S. Fatemi, Y. Futaana, and H. Nilsson (2012), The interaction between the Moon and the solar wind, *Earth Planets Space*, *64*(2), 237–245.
Hood, L. L., F. Herbert, and C. P. Sonett (1982), The deep lunar electrical conductivity profile: Structural and thermal inferences, *J. Geophys. Res.*, *87*(B7), 5311–5326.
Hood, L. L., D. L. Mitchell, R. P. Lin, M. H. Acuna, and A. B. Binder (1999), Initial measurements of the lunar induced magnetic dipole moment using Lunar Prospector Magnetometer data, *Geophys. Res. Lett.*, *26*(15), 2327–2330.
Khan, A. (2002), An inquiry into the lunar interior: A nonlinear inversion of the Apollo lunar seismic data, *J. Geophys. Res.*, *107*(E6), 5036, doi:10.1029/2001JE001658.
Khan, A., J. D. Connolly, N. Olsen, and K. Mosegaard (2006), Constraining the composition and thermal state of the moon from an inversion of electromagnetic lunar day-side transfer functions, *Earth Planet. Sci. Lett.*, *248*(3–4), 579–598.
Khan, A., A. Pommier, G. A. Neumann, and K. Mosegaard (2013), The lunar moho and the internal structure of the Moon: A geophysical perspective, *Tectonophysics*, *609*, 331–352.
Lindkvist, J., M. Holmström, K. K. Khurana, S. Fatemi, and S. Barabash (2015), Callisto plasma interactions: Hybrid modeling including induction by a subsurface ocean, *J. Geophys. Res. Space Physics*, *120*, 4877–4889, doi:10.1002/2015JA021212.
Lognonné, P., J. Gagnepain-Beyneix, and H. Chenet (2003), A new seismic model of the Moon: Implications for structure, thermal evolution and formation of the Moon, *Earth Planet. Sci. Lett.*, *211*(1–2), 27–44.
Lyon, E. F., H. S. Bridge, and J. H. Binsack (1967), Explorer 35 plasma measurements in the vicinity of the Moon, *J. Geophys. Res.*, *72*(23), 6113–6117.
Nakamura, Y., G. Latham, D. Lammlein, M. Ewing, F. Duennebier, and J. Dorman (1974), Deep lunar interior inferred from recent seismic data, *Geophys. Res. Lett.*, *1*(3), 137–140.
Nakamura, Y., F. K. Duennebier, G. V. Latham, and H. J. Dorman (1976), Structure of the lunar mantle, *J. Geophys. Res.*, *81*(26), 4818–4824.
Neubauer, F. M. (1999), Alfvén wings and electromagnetic induction in the interiors: Europa and Callisto, *J. Geophys. Res.*, *104*(A12), 28,671–28,684.
Omidi, N., X. Blanco-Cano, C. T. Russell, H. Karimabadi, and M. Acuna (2002), Hybrid simulations of solar wind interaction with magnetized asteroids: General characteristics, *J. Geophys. Res.*, *107*(A12), 1487, doi:10.1029/2002JA009441.
Russell, C. T., and B. R. Lichtenstein (1975), On the source of lunar limb compressions, *J. Geophys. Res.*, *80*(34), 4700–4711.
Russell, C. T., P. J. Coleman, and G. Schubert (1974), Lunar magnetic field: Permanent and induced dipole moments, *Science*, *186*(4), 825–826.
Russell, C. T., P. J. Coleman, and B. E. Goldstein (1981), Measurements of the lunar induced magnetic moment in the geomagnetic tail—Evidence for a lunar core, in *Proceedings of 12th Lunar and Planetary Science Conference, Houston, Tex., March 16–20, 1981*, vol. 12, pp. 831–836, Pergamon Press, New York and Oxford.
Saur, J., F. M. Neubauer, and K.-H. Glassmeier (2010), Induced magnetic fields in solar system bodies, *Space Sci. Rev.*, *152*, 391–421.
Schubert, G., B. R. Lichtenstein, P. J. Coleman, and C. T. Russell (1974), Simultaneous Explorer 35 and Apollo 15 orbital magnetometer observations: Implications for lunar electrical conductivity inversions, *J. Geophys. Res.*, *79*(14), 2007–2013.
Shimizu, H., M. Matsushima, F. Takahashi, H. Shibuya, and H. Tsunakawa (2013), Constraint on the lunar core size from electromagnetic sounding based on magnetic field observations by an orbiting satellite, *Icarus*, *222*(1), 32–43.
Sonett, C. P. (1982), Electromagnetic induction in the Moon, *Rev. Geophys.*, *20*(3), 411–455.
Sonett, C. P., and D. S. Colburn (1968), The principle of solar wind induced planetary dynamos, *Phys. Earth Planet. Inter.*, *1*(5), 326–346.
Tauxe, L., S. K. Banerjee, R. F. Butler, and R. Van der Voo (2014), *Essentials of Paleomagnetism*, 3rd Web ed., Univ. of Calif. Press, Calif.
Weber, R. C., P.-Y. Lin, E. J. Garnero, Q. Williams, and P. Lognonné (2011), Seismic detection of the lunar core, *Science*, *331*, 309–312.
Whang, Y. C., and N. F. Ness (1970), Observations and interpretation of the lunar Mach cone, *J. Geophys. Res.*, *75*(31), 6002–6010.
Wieczorek, M. A., et al. (2006), The constitution and structure of the lunar interior, *Rev. Mineral. Geochem.*, *60*(1), 221–364.
Wieczorek, M. A., et al. (2013), The crust of the Moon as seen by GRAIL, *Science*, *339*(6120), 671–675.
Williams, J. G., D. H. Boggs, C. F. Yoder, J. T. Ratcliff, and J. O. Dickey (2001), Lunar rotational dissipation in solid body and molten core, *J. Geophys. Res.*, *106*(E11), 27,933–27,968, doi:10.1029/2000JE001396.
Williams, J. G., et al. (2014), Lunar interior properties from the GRAIL mission, *J. Geophys. Res. Planet*, *119*, 1546–1578, doi:10.1002/2013JE004559.
Zhang, H., K. K. Khurana, M. G. Kivelson, V. Angelopoulos, W. X. Wan, L. B. Liu, Q. G. Zong, Z. Y. Pu, Q. Q. Shi, and W. L. Liu (2014), Three-dimensional lunar wake reconstructed from ARTEMIS data, *J. Geophys. Res. Space Physics*, *119*, 5220–5243, doi:10.1002/2014JA020111.